AIAA AVIATION Forum
17-21 June 2019, Dallas, Texas
AIAA Aviation 2019 Forum

10.2514/6.2019-3495

Improving Efficiency of Co-Flow Jet Micro-Compressor Actuator Outlet Guide Vanes and Nozzle

Kewei Xu *, Gecheng Zha †
Dept. of Mechanical and Aerospace Engineering
University of Miami, Coral Gables, Florida 33124
E-mail: gzha@miami.edu

Abstract

This paper conducts the numerical design of the outlet guide vanes (OGV) and nozzle for a Co-flow Jet (CFJ) micro-compressor actuator to maximize the efficiency. For CFJ active flow control, the embedded micro-compressor actuator is required to produce the static pressure ratio (π_{s-t}) lower than 1 to match the low pressure of CFJ airfoil leading edge suction peak. Therefore, a high efficiency outlet guide vane with a nozzle designed to deswirl the flow and decrease the outlet static pressure. Parametric studies of the OGV deswirl angle and flow path geometrical parameters are studied including: the flow path diverging location and diverging angle for the OGV, the flow path converging location and converging angle for the nozzle. The numerical results show that for the OGV, a flow path with a 7° front diverging (33%) is beneficial to decrease the OGV outlet Mach number. For the nozzle downstream of the OGV, a 10° rear converging location at 80% streamwise length is able to achieve the targeted static pressure ratio of 0.987 with a minimum loss. It is also found that deswirling by the vanes with a converging nozzle helps to reduce the vane loading and loss. The final optimized compressor has outlet swirl angle of 5.45°, total pressure recovery of 98.7% and compressor efficiency of 75.05%. The efficiency analysis of a low pressure ratio compressor is conducted. In addition to the stage efficiency and total pressure recovery of OGV and nozzle, it is found that a higher stage total pressure ratio is beneficial to achieve a higher full compressor efficiency. The full compressor efficiency is sensitive to the total pressure recovery of the OGV and outlet duct. For the present design with the stage pressure ratio of 1.13, if the total pressure recovery drops from 0.99 to 0.98 by one point, it costs the full compressor efficiency loss by 8 points from 77% to 69%. It is hence crucial to have an efficient design of the OGV and outlet duct. The penalty is decreased if the stage total pressure ratio is increased.

Nomenclature

AoA	Angle of attack
AFC	Active flow control
CFJ	Co-flow jet
D	Diameter
LE	Leading edge
$\dot{m}$	Mass flow
Ma	Mach number

* Ph.D. Student
† Professor, ASME Fellow, AIAA associate Fellow

OGV	Outlet guide vane
$\dot{Q}$	Volume flow rate
$RANS$	Reynolds-Averaged Navier-Stokes
Re	Reynolds number
RPM	Round per second
SSR	Shear strain rate
TE	Trailing edge
U	Circumferential speed
$ZNMF$	Zero-net mass flux
c	Subscript, stands for corrected
j	Subscript, stands for jet
t	Subscript, stands for tip
$s-t$	Subscript, stands for static to total
0	Subscript, stands for total
1	Subscript, stands for impeller inlet
2	Subscript, stands for impeller outlet
$2t$	Subscript, stands for impeller outlet tip
ω_s	Specific speed
γ	Air specific heats ratio
τ	Shear stress
η	Micro-comprssor efficiency ($\eta = \frac{[p_{tr}^{(\frac{\gamma-1}{\gamma})}-1]}{T_{tr}-1}$)
π	Pressure ratio
ϕ	Flow coefficient ($\frac{\dot{Q}_1}{D_{2t}^2 U_{2t}}$)

1 Introduction

Mixed flow compressors are able to achieve both high mass flow rate and high pressure rise, which combines the merits of axial and centrifugal compressors. Recently, increasing attention is paid to mixed compressor design driven by the interest of more and more micro-compressor applications, in particular in the field of active flow control.

Musgrave and Plehn [1] designed a single stage mixed flow compressor with a pressure ratio of 3.02 and the rotor efficiency of 0.91. Monig et al [2, 3] studied the mixed flow impeller with a pressure ratio of 5. Their experimental results suggested that a high outlet Mach number is unfavorable for downstream diffuser. A high-specific speed (ω_s) centrifugal compressor with ω_s of 1.8 was designed by Rodgers [4]. It set the benchmark that represented the performance potential of high ω_s centrifugal compressor. Casey et al [5] developed a new equation for Cordier line in the mixed flow region, which provided a guideline for the preliminary design of mixed flow compressors. They then designed a transonic mixed flow compressor stage with a very high flow coefficient of 0.25 and an isentropic pressure rise coefficient of 0.56 [6]. The effects of Reynolds number on centrifugal and mixed-flow compressor were also studied [7, 8, 9, 10]. Previous studies are more focused on the mixed flow compressor with high loading, but not much attention is paid to the mixed flow compressors with low enthalpy rise, high mass flow rate and low static pressure ratio which has great application potential as actuators for Co-flow Jet (CFJ) active flow control (AFC).

Among various AFC techniques, Co-flow Jet is a zero-net mass-flux (ZNMF) flow control method recently

developed by Zha et al. [11, 12, 13, 14, 15, 16, 17, 18, 19, 20, 21, 22, 23]. It is demonstrated numerically and experimentally that CFJ achieves significant improvements on airfoil lift augmentation, drag reduction and stall margin enlargement.

In a CFJ airfoil, electric micro-compressors along with suction and injection ducts are embedded inside the airfoil as shown in Fig. 1. The micro-compressor works as an actuator that draws flow near trailing edge (TE), pressurizes the flow and ejects it as a jet near leading edge (LE).

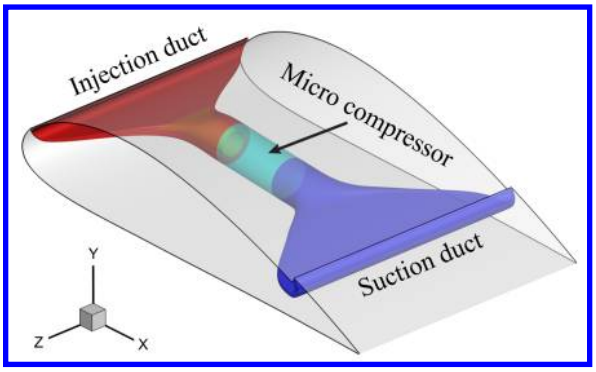

Figure 1: Schematics of the CFJ airfoil with embedded micro-compressor

Such application of CFJ actuators poses a special requirement for the micro-compressor design: The required static pressure ratio (π_{s-t}) lower than 1 to match the low pressure of CFJ airfoil leading edge suction peak. Total pressure and static pressure are typically increased simultaneously through compressor. However, CFJ actuator is required to increase the total pressure to compensate the loss and decrease the static pressure to match the airfoil leading edge suction pressure. Therefore, a high efficiency outlet guide vane with a nozzle is required at compressor outlet to decrease the outlet static pressure.

2 Computational Setup

The 3D RANS simulation is conducted using ANASYS CFX code. The computational domain is a single passage with multi-blade rows, which consists of the a converging intake, an impeller passage, a stator passage and an OGV passage with a downstream nozzle. Fig. 2 shows the structured mesh with a size of 720000 nodes generated by Turbogrid. The rotor mesh has 50 points spanwise and 9 points in the tip clearance. The mesh refinement study indicates that the results are converged based on the mesh size. Turbulent effects are simulated by the k-ϵ model with scalable wall function. The mixing interface boundary conditions are applied on the interfaces between blade rows. The convergence criterion is that the residual reduced by 4 orders of magnitude.

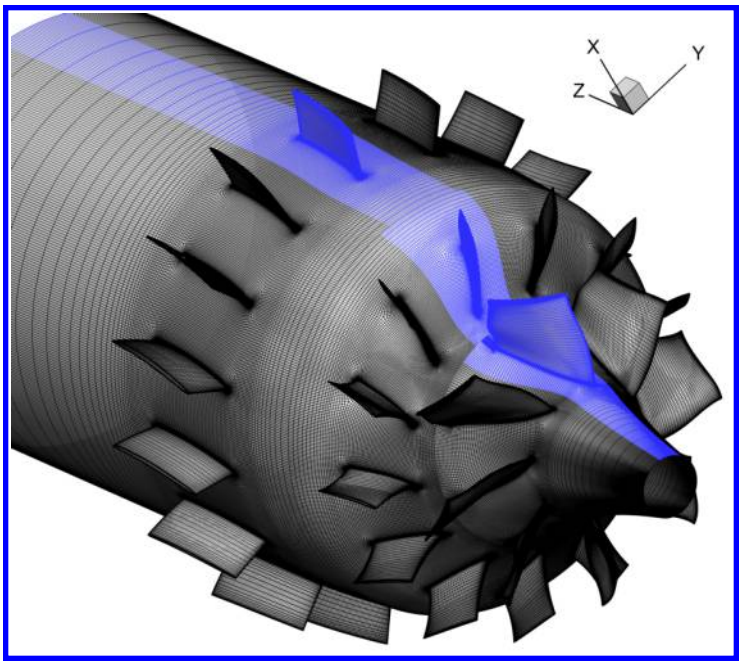

Figure 2: Computational domain of micro-compressor simulation

3 Computational Approach Validation

A micro-compressor with the similar size and Reynolds number designed by PCA [24], manufactured and tested by Celeroton [25] is used to validate the simulation approach. The validated micro-compressor is also a mixed-compressor with a similar configuration as shown in Fig. 3, including impeller, stator, OGV and outlet duct, but it has substantially lower mass flow rate and power than the micro-compressor used in the present study [26]. The computed speedlines compared with the measured data for both the total pressure ratio and efficiency versus the normalized mass flow rate are shown in Fig. 4, for which the mass flow rate is normalized by the design point mass flow rate.

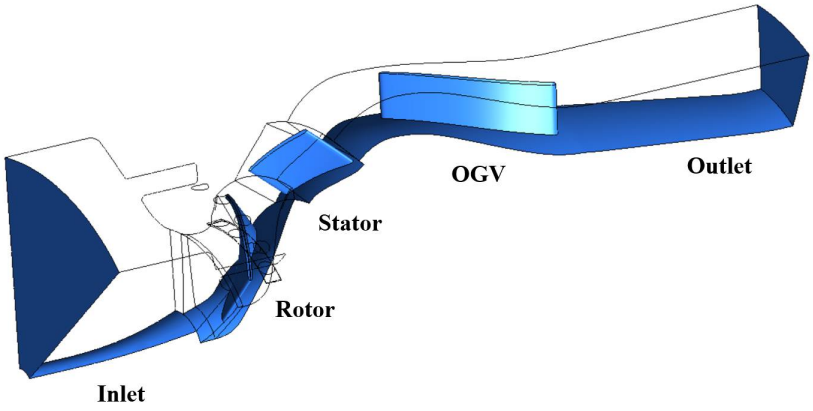

Figure 3: The configuration of the validated micro-compressor

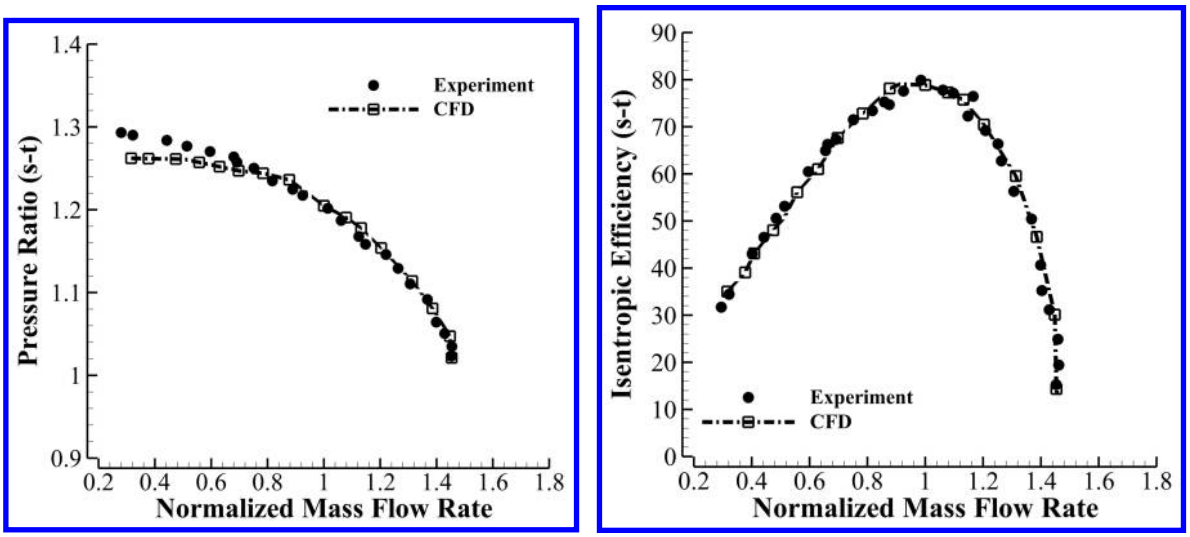

(a) Total pressure ratio (b) Isentropic efficiency

Figure 4: Validation of design tool

Overall, the predicted results agree very well with experimental ones, especially at the design point (normalized mass flow rate of 1.0). The maximum deviation between the computation and testing is the near stall total pressure ratio, which is less than 3%. The deviation is mostly due to the flow separation and complex vortical flow, for which the RANS turbulence model is unable to resolve.

4 Results and Discussions

Fig. 5 is the computed streamlines and the surface pressure contour of the micro-compressor used in the present study [26]. The rotor consists of 8 blades and the stator consists of 13 blades. Front loaded rotor blade work distribution is adopted for the blade shape design and the spanwise free vortex work distribution is applied to reduce spanwise mixing loss. Without OGV and nozzle, the stage efficiency achieved is 84.3% with a total pressure ratio of 1.13 and flow coefficient (ϕ) of 0.3. The computed stage performance of total pressure ratio and isotropic efficiency are shown in Fig. 6.

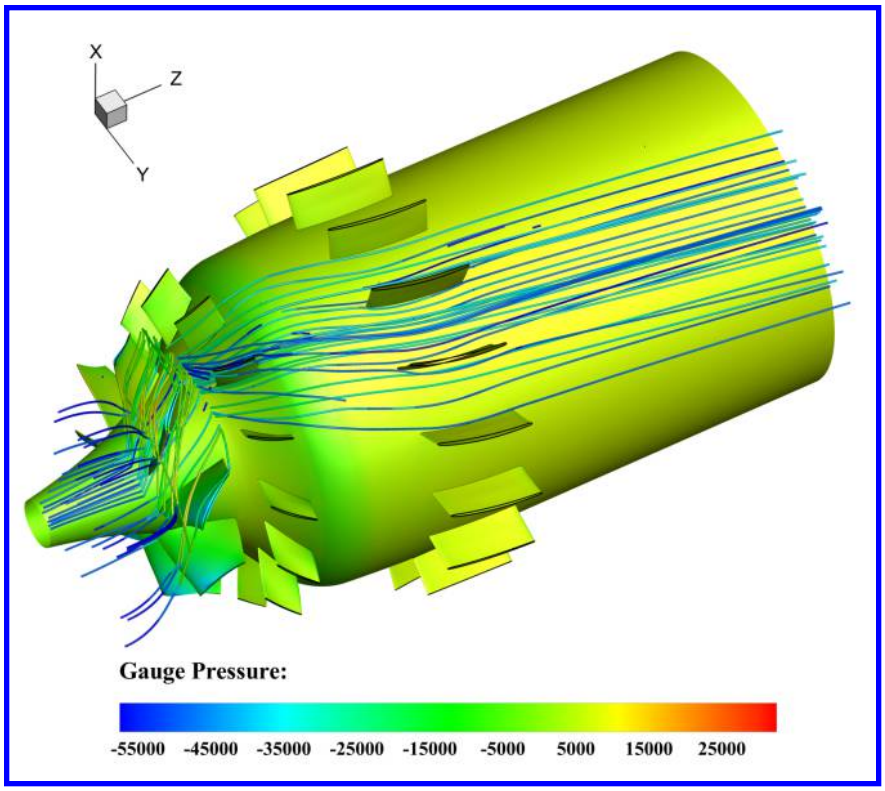

Figure 5: Pressure contour at compressor surface

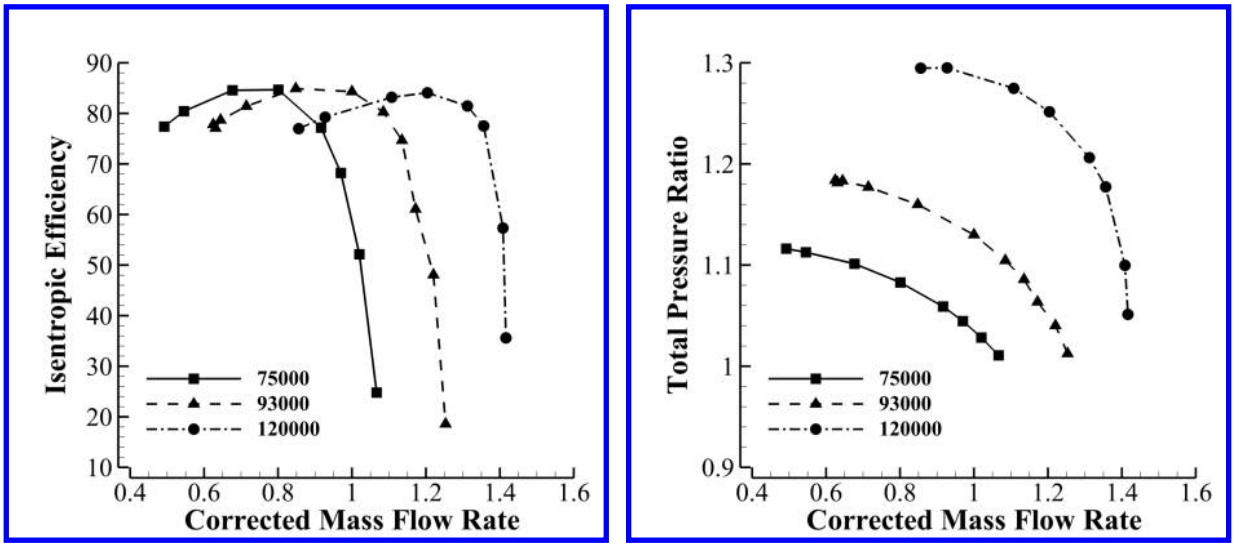

(a) Isentropic efficiency (b) Total pressure ratio

Figure 6: Stage performance at different RPM

The scope of the present design is illustrated in Fig. 7, which is the meridional view of the micro-compressor flow path. The terminology used in this paper is also illustrated in Fig. 7. The term "compressor stage" stands for the core compressor without the OGV and the outlet duct. The "compressor" or "full compressor" means the whole system with the compressor stage and the outlet duct and OGV.

The present design starts from the outlet of stator where the flow is turned to axial as shown in Fig. 7. The geometrical parameters for the flow path trade study include the diverging location, diverging angle, converging location and converging angle as illustrated in Fig. 7. Three locations for diverging and converging with different streamwise length from compressor inlet are examined, namely: front (33%), middle (58%), rear (80%).

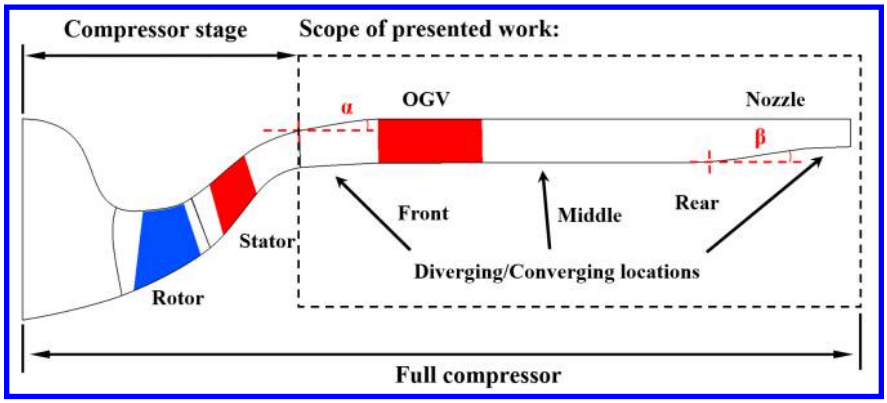

Figure 7: Variables illustration for meridional channel design

The OGV with a straight outlet duct is used as the starting design to analyze the loss source of OGV and nozzle. Fig. 8 (a) presents the mass averaged total pressure contours on the meridional plane. It can be observed that the total pressure is dissipated quickly as flow approaches downstream. The total pressure recovery of the OGV with the outlet duct is 99.06%, which decreases the isentropic efficiency of the compressor by 9.6%. To create a reference to see the outlet duct effect only, a simulation is done without the OGV blades and the flow swirl. The total pressure recovery is 98.0% in the contours shown in Fig. 8 (b), which is slightly higher than the one with the OGV 97.8% shown in Fig. 8 (a). Denton [27] studied the loss mechanism in turbomachines, for which the vicious shear stress work is identified as the main cause for entropy increase and energy loss.

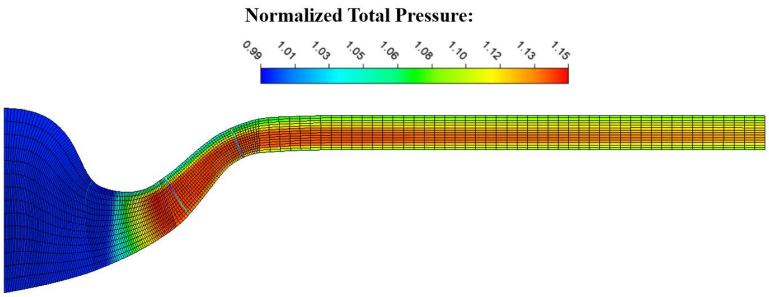

(a) OGV and nozzle in straight channel

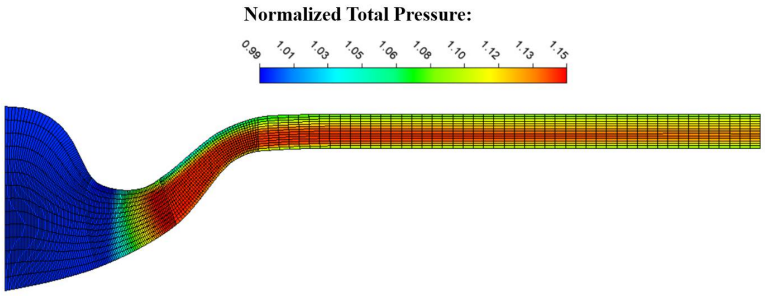

(b) OGV and nozzle without OGV vanes in straight channel

Figure 8: Starting Design

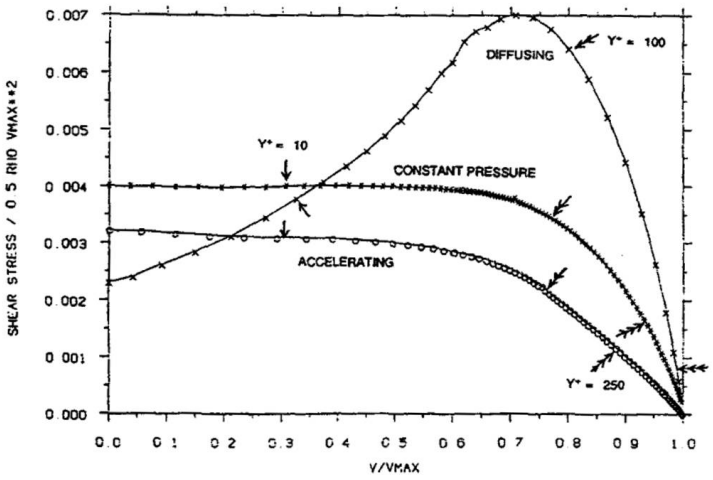

Figure 9: Variation of shear stress with velocity across a boundary layer (adopted from [27])

Fig. 9 shows the relationship between normalized shear stress (τ) and velocity. The area under τ-V curve can be interpreted as the viscous shear stress work and is proportional to the rate of entropy creation. The larger the area, the higher the entropy rise. As it indicates in Fig. 9 that a boundary layer with diffusing flow and adverse pressure gradient increases the shear stress coefficient defined as $\tau/(0.5\rho \cdot V_{max}^2)$, especially as velocity approaches 70% of the freestream velocity, whereas a boundary layer with an accelerating flow and favorable pressure gradient

generates lower shear stress. Such behavior suggests that a converging flow path decreases viscous loss. However, the non-dimensional shear stress in Fig. 9 is normalized by the square of the freestream velocity. This suggests if the freestream velocity is high enough, the viscous shear stress in an accelerating boundary layer can exceed that of a diffusing boundary layer. In other words, decreasing the freestream velocity by diffusing the flow may reduce the friction loss. However, diffusing also generates adverse pressure gradient and increases the shear stress coefficient . Therefore, a balance between converging and diverging the flow path needs to be achieved to minimize the loss.

Shear strain rate (SSR) is used here to represent the shear stress [10]. It is linearly proportional to shear stress with temperature held constant and is defined as $\left[2\frac{\partial U_i}{\partial X_j}S_{ij}\right]^{\frac{1}{2}}$, which represents the deformation of fluid partial due to velocity gradient. In the present study, the SSR is normalized by the OGV inlet mass averaged SSR.

4.1 Diverging Location and Angle

For the diverging angle and location studies, the flow path area is diverged by increasing the casing radius because the hub radius is constrained by the embedded motor and can't be decreased. Casing radius is also limited by a maximum value. After diverging, the same area ratio of 1.38 is achieved among all studied cases. Fig. 10, Fig. 11 and Fig. 12 are the results of different diverging location, in which the contours of mass averaged shear strain rate, velocity and entropy on the meridional plane are presented. It is found that front diverging at 33% streamwise location has the best performance with an isentropic efficiency of 76.2% achieved. The reason can be explained by the following analysis. Fig. 10 (a) shows that the front diverging deaccelerates the flow without separation. The decreased flow velocity produced lower shear strain rate at the wall, which indicates a mitigated viscous effect, as shown in Fig. 11 (a). The reduced shear stress together with low velocity generates lower entropy creation rate as shown in Fig. 12. The front diverging has a longer length of flow path with low speed flow and thus less entropy increase will be created. This explains why the front diverging has a better efficiency.

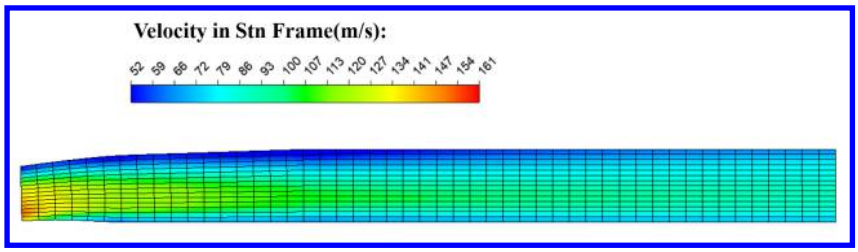

(a) Front diverging (33%)

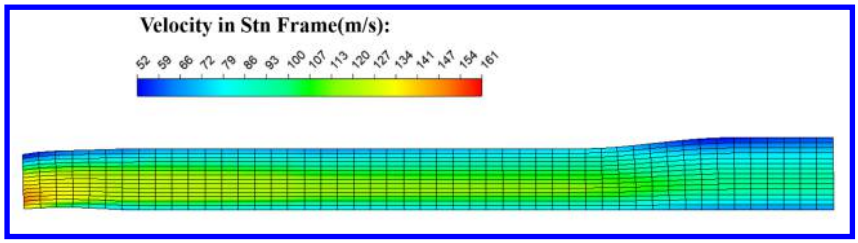

(b) Rear diverging (80%)

Figure 10: Meridional contours of mass averaged velocity of diverging OGV channel

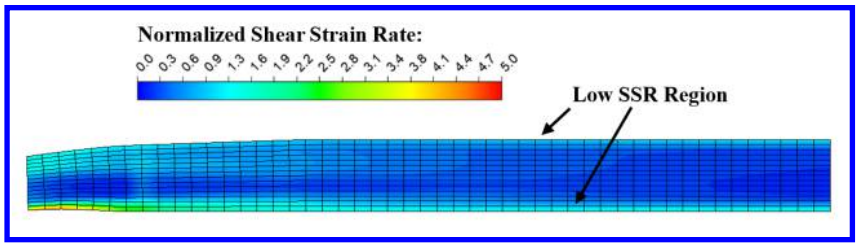

(a) Front diverging (33%)

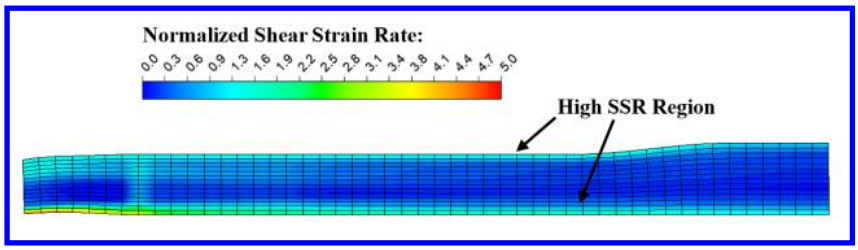

(b) Rear diverging (80%)

Figure 11: Meridional contours of mass averaged shear strain rate of diverging OGV channel

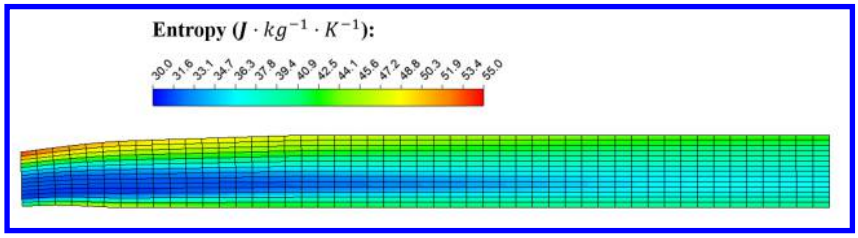

(a) Front diverging (33%)

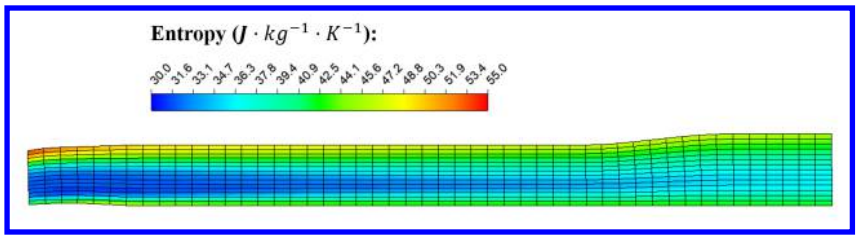

(b) Rear diverging (80%)

Figure 12: Meridional contours of mass averaged entropy of diverging OGV channel

Diverging angle studies are conducted at the 33% streamwise location, the optimum diverging location. Three diverging angles are studied: 4°, 7° and 10°. Fig. 13 and Fig. 14 shows the velocity contours and SSR contours of the three cases. It is found that the diverging angle has a minor effect on OGV loss, where the total pressure recovery varies 0.027% among the studied cases. The reason is that before the flow at casing enters OGV, it is already diffused by the up-stream stator. Therefore, there is not much room for further reducing the viscous loss by diffusing and decelerating flow. A 4° geometry has a relatively long diverging section, which increases friction loss with high mass flow rate. A 10° geometry diverges too rapidly and may induce separation at low mass flow rate condition. Thus, the medium diverging angle 7° is selected.

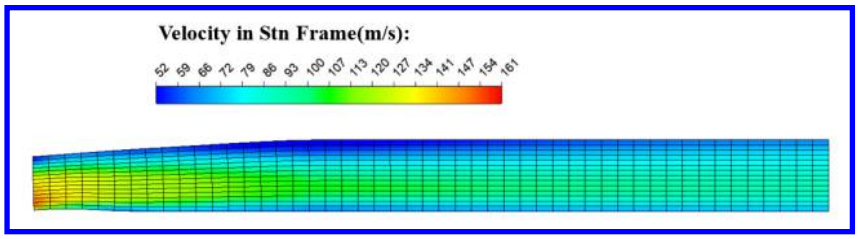

(a) 4° diverging OGV flow path

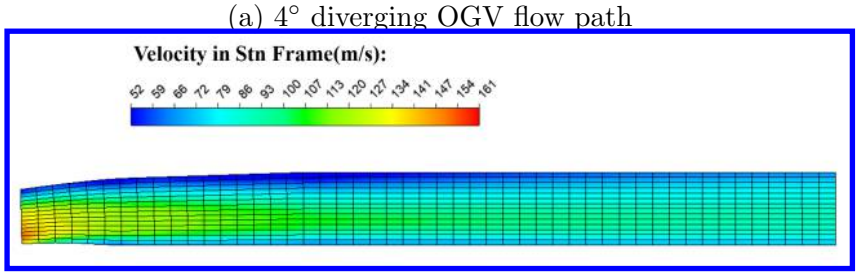

(b) 7° diverging OGV flow path

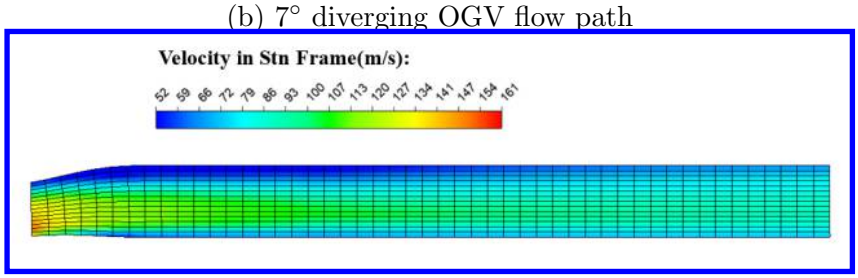

(c) 10° diverging OGV flow path

Figure 13: Meridional contours of mass averaged velocity of diverging OGV

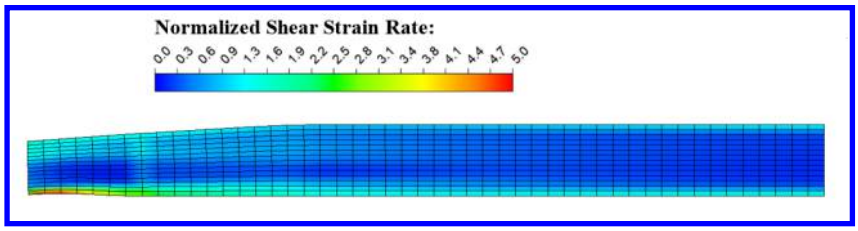

(a) 4° diverging OGV flow path

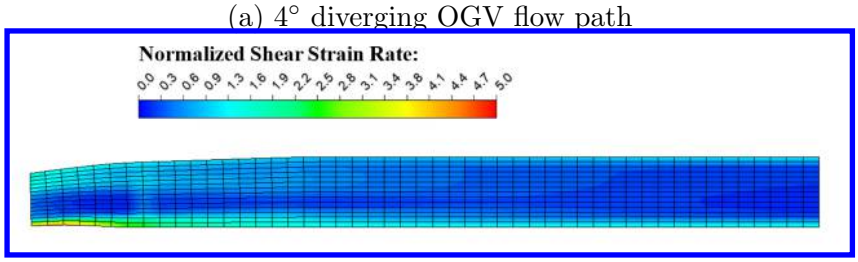

(b) 7° diverging OGV flow path

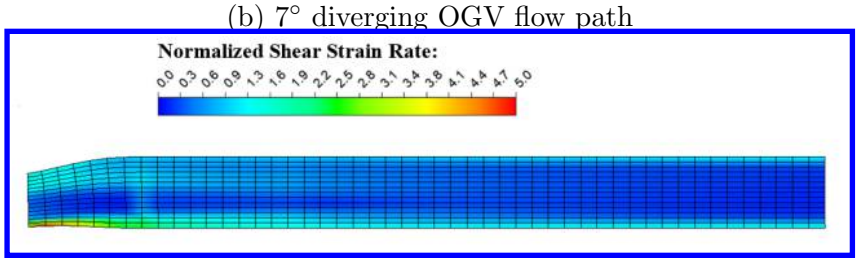

(c) 10° diverging OGV flow path

Figure 14: Meridional contours of mass averaged SSR of diverging OGV

4.2 Converging Location and Angle

For the converging location and angle studies, the flow path is converged by increasing hub radius and after converging, the same static pressure ratio of 0.987 is achieved. The results of converging location are presented in Fig. 15, Fig. 16 and Fig. 17. Efficiency is decreased due to the loss of the long outlet duct for all the cases, among which the rear converging duct has the minimum loss. Fig. 15 shows that early converging makes more area occupied by high speed flow because of nozzle acceleration. The wall SSR is largely increased in high speed region as shown in Fig. 15 (a) that the near hub SSR at nozzle outlet approaches 4.7, whereas the SSR at the same location in Fig. 15 (b) is only 1.3. The increment of SSR and velocity generates higher entropy as shown in Fig. 17, which decreases the duct efficiency.

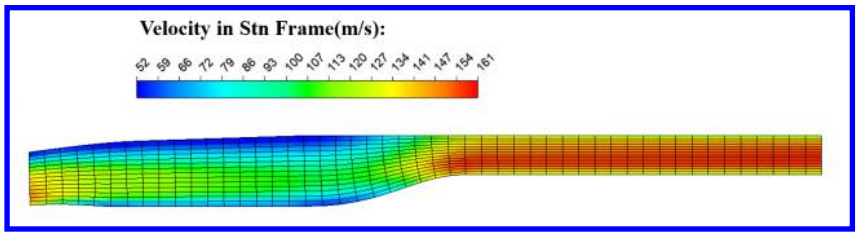

(a) Middle converging (58%)

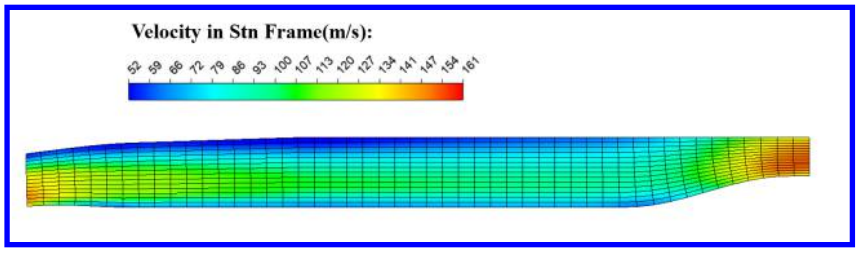

(b) Rear converging (80%)

Figure 15: Meridional contours of mass averaged velocity of converging nozzle

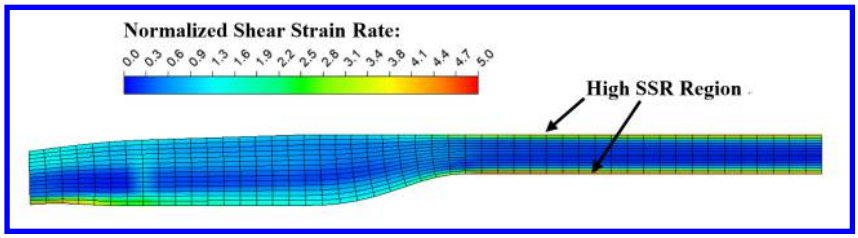

(a) Middle converging (58%)

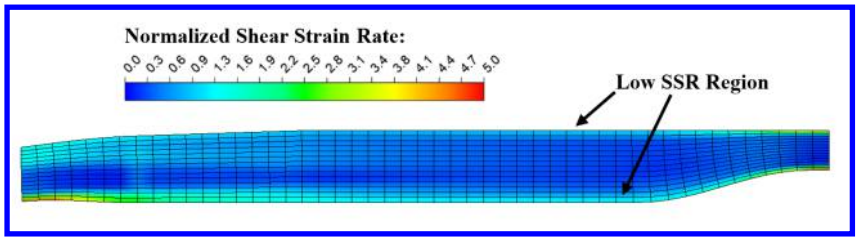

(b) Rear converging (80%)

Figure 16: Meridional contours of mass averaged shear strain rate of converging nozzle

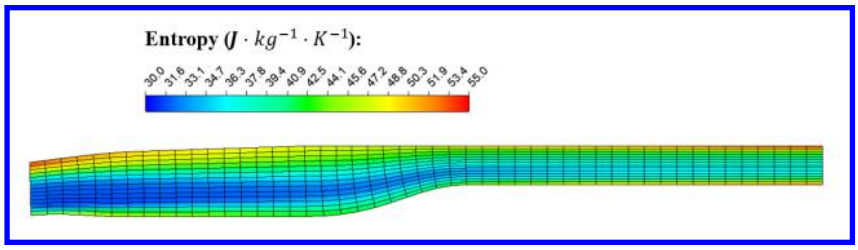

(a) Front diverging (33%)

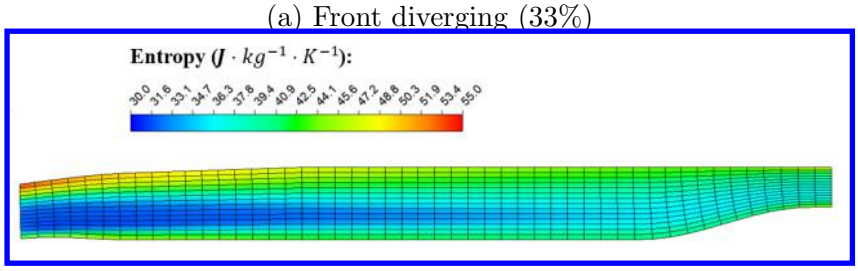

(b) Rear diverging (80%)

Figure 17: Meridional contours of mass averaged entropy of converging nozzle

At rear converging location, three converging angles of 10°, 7° and 4° are studied and the results are shown in Fig. 19 and Fig. 18. The OGV flow path with 10° converging angle achieves the lowest loss and creates the best efficiency of 75.03% of the whole micro-compressor system. It is because a higher converging angle accelerates the flow in a short distance, which decreases the high speed flow path length and reduces viscous loss.

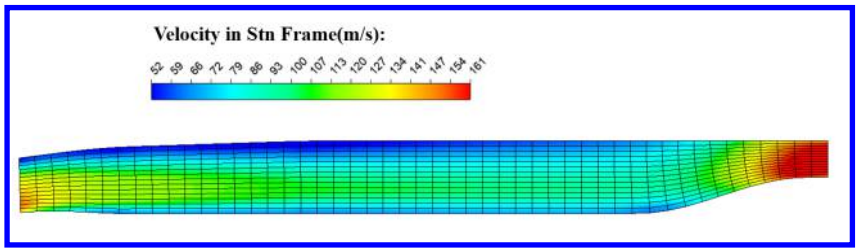

(a) 10° converging nozzle

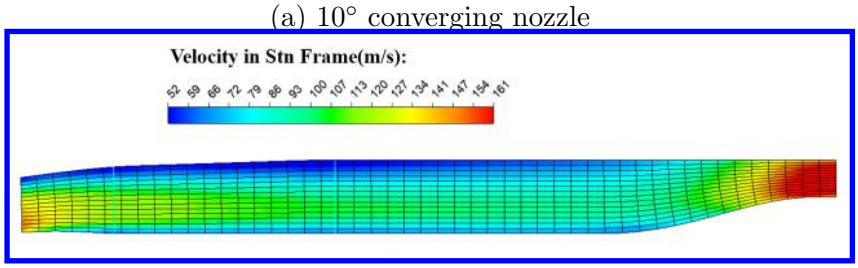

(b) 7° converging nozzle

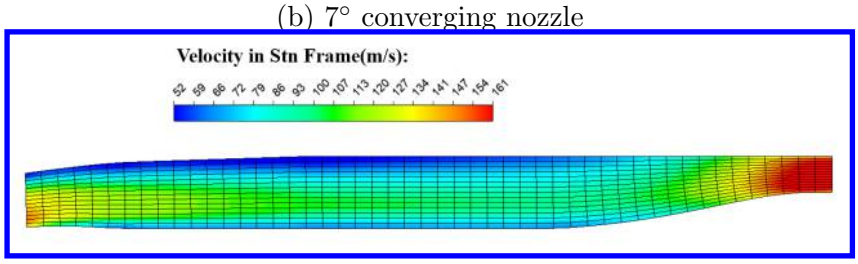

(c) 4° converging nozzle

Figure 18: Meridional contours of mass averaged velocity of converging nozzle

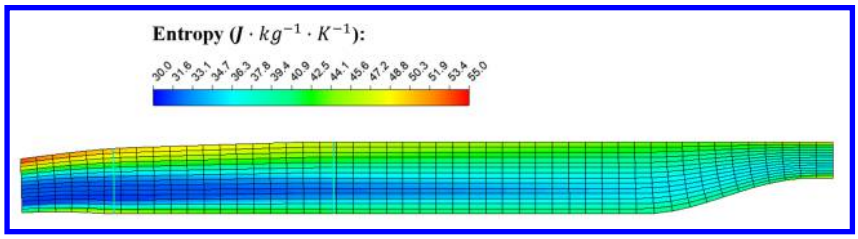

(a) 10° converging nozzle

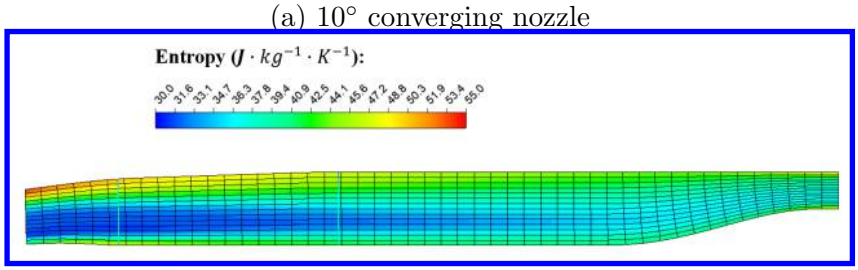

(b) 7° converging nozzle

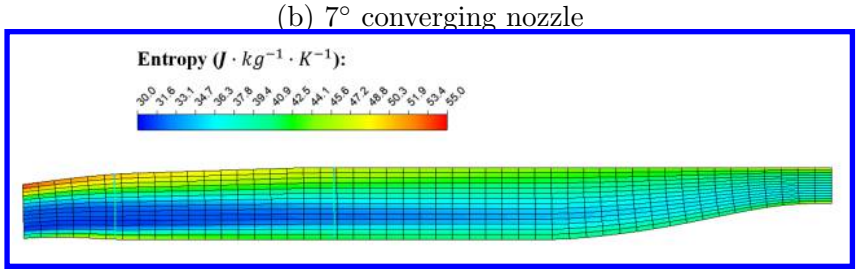

(c) 4° converging nozzle

Figure 19: Meridional contours of mass averaged entropy of converging nozzle

4.3 OGV Swirl

The swirl angle is required to be less than 6° at compressor outlet. Two deswirl methods are studied: one is to deswirl only by guide vanes; the other one is to deswirl by the vanes with a converging nozzle. It is found that both methods can achieve target swirl angle. However, the isentropic efficiency of the second method is 75.03%, which is 1.03% higher than the vanes only method. This is because deswirling only by vanes increases the vane loading, which intensifies vane surface adverse pressure gradient and induces separation loss. Fig. 20 shows the flow tends to separate at low and high span of guide vane trailing edge. Therefore, the combining method is selected and the averaged swirl angle at compressor outlet is 5.45°.

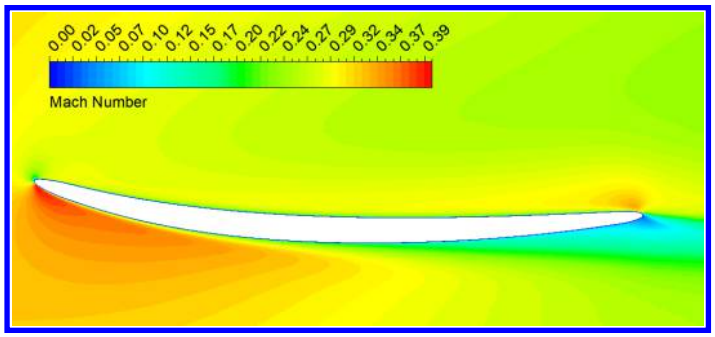

(a) Mach number contour at 15% span

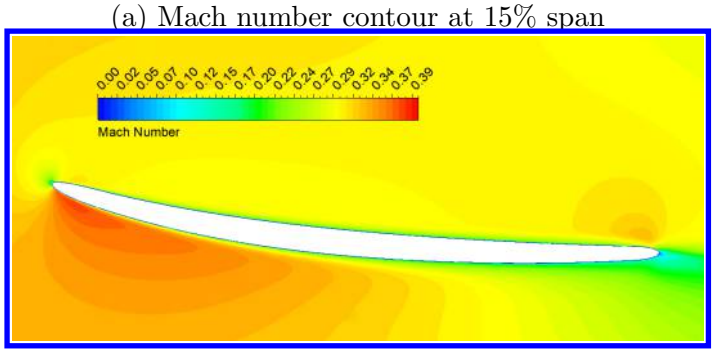

(b) Mach number contour at 50% span

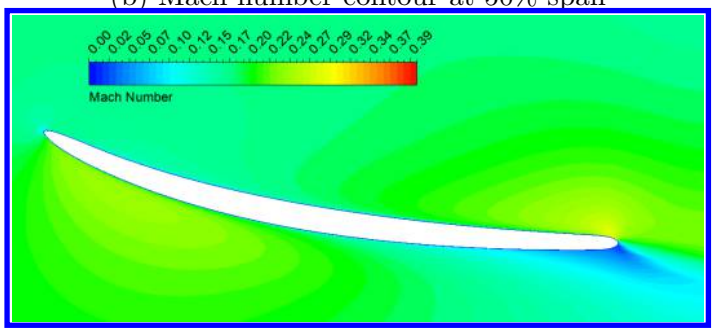

(c) Mach number contour at 85% span

Figure 20: Mach number contours of OGV vane

4.4 Compressor Efficiency Analysis

Finally, the optimized OGV and nozzle is obtained with 7° front diverging, 10° rear converging flow path and outlet swirl angle achieved is 5.45°. The optimized geometry achieves isentropic efficiency of 75.03% with the outlet OGV-duct total pressure recovery ratio of 98.7%. Compared with the preliminary design that doesn't has diverging and converging flow path, the overall improvement of isentropic efficiency is 1.3%. Even though the outlet-OGV total pressure recovery of 98.7% is fairly high, the efficiency of the full compressor is largely determined by the core single stage compressor ratio as explained below. The terminology defined for Fig. 7 is used below to define the compressor stage as the core single stage compressor. The full compressor is defined as the core compressor with the OGV and outlet duct.

The isentropic efficiency (η) of the full compressor, including OGV and outlet nozzle is expressed as :

$$\eta = \frac{[p_{tr}^{(\frac{\gamma-1}{\gamma})} - 1]}{T_{tr} - 1} \tag{1}$$

where p_{tr} and T_{tr} are the total pressure ratio and total temperature ratio of the full compressor.

Since,

$$p_{tr} = p_{tr0} \cdot \delta \tag{2}$$

where p_{tr0} is the compressor stage total pressure ratio and δ is the total pressure recovery of OGV and nozzle.

Adiabatic process is considered for the OGV and outlet duct. Thus, the stage total temperature rise is equal to the full compressor total temperature rise. Following the definition of the stage efficiency, T_{tr} can be expressed as:

$$T_{tr} - 1 = T_{tr0} - 1 = (p_{tr0}^{(\frac{\gamma-1}{\gamma})} - 1)/\eta_0 \tag{3}$$

where η_0 is the single stage compressor efficiency.

Substituting Eq. (2) and Eq. (3) in Eq. (1), the compressor efficiency can be expressed as:

$$\eta = \frac{[(p_{tr0} \cdot \delta)^{(\frac{\gamma-1}{\gamma})} - 1]\eta_0}{p_{tr0}^{(\frac{\gamma-1}{\gamma})} - 1} \tag{4}$$

Simplified as:

$$\eta = \eta_0 \cdot \delta^{(\frac{\gamma-1}{\gamma})} + \frac{(\delta^{(\frac{\gamma-1}{\gamma})} - 1)\eta_0}{p_{tr0}^{(\frac{\gamma-1}{\gamma})} - 1} \tag{5}$$

The compressor efficiency is related to the compressor stage total pressure ratio (p_{tr0}), OGV total pressure recovery (δ) and stage efficiency (η_0). To study the effect of p_{tr0} only, δ and η_0 are treated as constants. Thus, Eq. (5) can be simplified as:

$$\eta = C_1 - \frac{C_2}{p_{tr0}^{(\frac{\gamma-1}{\gamma})} - 1} \tag{6}$$

where $C_1 = \eta_0 \cdot \delta^{(\frac{\gamma-1}{\gamma})}$, and $C_2 = (1 - \delta^{(\frac{\gamma-1}{\gamma})})\eta_0$. In Eq. (6), p_{tr0} is always greater than 1 and C_1 and C_2 are always positive. As p_{tr0} increases, η is also increased. Fig. 21 plots η versus p_{tr0} based on Eq. (6) with δ=0.980, 0.987 and 0.990 and η_0=84.3%. As the plots show that the compressor with higher total pressure ratio will have the overall higher efficiency than the one with lower total pressure ratio, even though they both possess the same total pressure recovery ratio and stage efficiency. For the present design, the p_{tr0} is 1.13 and the δ is 0.987, which falls on the predicted point marked as red star in Fig. 21. Fig. 21 also indicates that the total pressure recovery of the outlet and OGV has significant effect on the efficiency of the full compressor. For the present design with

the stage pressure ratio of 1.13, if the total pressure recovery drops from 0.99 to 0.98 by one point, it costs the full compressor efficiency loss by 8 points from 77% to 69%. It is hence crucial to have an efficient design of the OGV and outlet duct. The penalty is decreased if the stage total pressure ratio is increased.

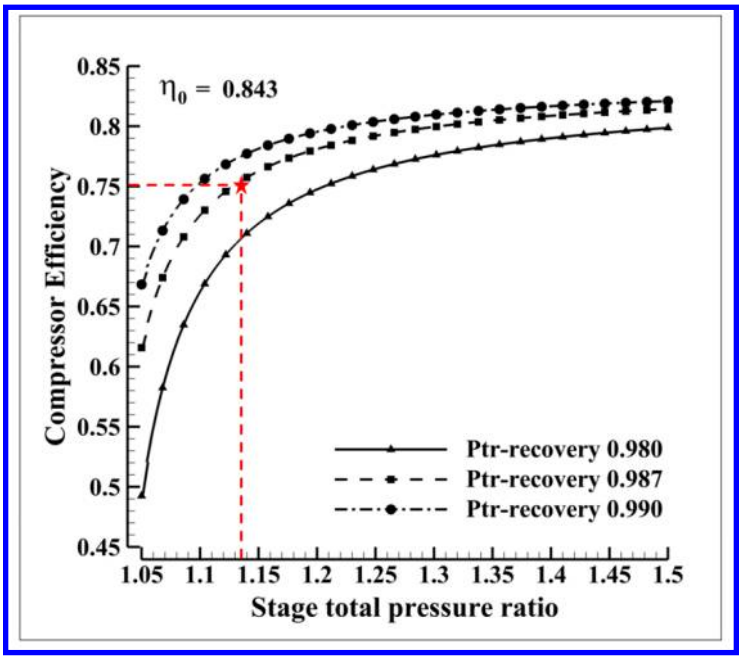

Figure 21: Plots of compressor isentropic efficiency versus stage total pressure ratio

5 Conclusions

This paper conducts the numerical design of the outlet guide vanes (OGV) and nozzle for a Co-flow Jet (CFJ) micro-compressor actuator to maximize the efficiency. For CFJ active flow control, the embedded micro-compressor actuator is required to produce the static pressure ratio (π_{s-t}) lower than 1 to match the low pressure of CFJ airfoil leading edge suction peak. Therefore, a high efficiency outlet guide vane with a nozzle designed to deswirl the flow and decrease the outlet static pressure. Parametric studies of the OGV deswirl angle and flow path geometrical parameters are studied including: the flow path diverging location and diverging angle for the OGV, the flow path converging location and converging angle for the nozzle. The numerical results show that for the OGV, a flow path with a 7° front diverging (33%) is beneficial to decrease the OGV outlet Mach number. For the nozzle downstream of the OGV, a 10° rear converging location at 80% streamwise length is able to achieve the targeted static pressure ratio of 0.987 with a minimum loss. It is also found that deswirling by the vanes with a converging nozzle helps to reduce the vane loading and loss. The final optimized compressor has outlet swirl angle of 5.45°, total pressure recovery of 98.7% and compressor efficiency of 75.05%. The efficiency analysis of a low pressure ratio compressor is conducted. In addition to the stage efficiency and total pressure recovery of OGV and nozzle, it is found that a higher stage total pressure ratio is beneficial to achieve a higher full compressor efficiency. The full compressor efficiency is sensitive to the total pressure recovery of the OGV and outlet duct. For the present design with the stage pressure ratio of 1.13, if the total pressure recovery drops from 0.99 to 0.98 by one point, it costs the full compressor efficiency loss by 8 points from 77% to 69%. It is hence crucial to have an efficient design of the OGV and outlet duct. The penalty is decreased if the stage total pressure ratio is increased.

References

[1] D. Musgrave and N. Plehn, "Mixed-flow compressor stage design and test results with a pressure ratio of 3: 1," *Journal of turbomachinery*, vol. 109, no. 4, pp. 513–519, 1987.

[2] R. Mönig, K. Broichhausen, and H. Gallus, "Application of highly loaded single-stage mixed flow compressors in small jet-engines," tech. rep., MOTOREN-UND TURBINEN-UNION GMBH MUNICH (GERMANY FR), 1987.

[3] R. Mönig, W. Elmendorf, and H. Gallus, "Design and rotor performance of a 5: 1 mixed-flow supersonic compressor," in *ASME 1992 International Gas Turbine and Aeroengine Congress and Exposition*, pp. V001T01A040–V001T01A040, American Society of Mechanical Engineers, 1992.

[4] C. Rodgers, "Development of a high specific speed centrifugal compressor," in *ASME 1996 International Gas Turbine and Aeroengine Congress and Exhibition*, pp. V001T01A087–V001T01A087, American Society of Mechanical Engineers, 1996.

[5] M. Casey, C. Zwyssig, and C. Robinson, "The cordier line for mixed flow compressors," in *ASME Turbo Expo 2010: Power for Land, Sea, and Air*, pp. 1859–1869, American Society of Mechanical Engineers, GT2010-22549.

[6] H. Hazby, M. Casey, R. Numakura, and H. Tamaki, "A transonic mixed flow compressor for an extreme duty," *Journal of Turbomachinery*, vol. 137, no. 5, p. 051010, 2015.

[7] M. Casey and C. Robinson, "A unified correction method for reynolds number, size, and roughness effects on the performance of compressors," *Proceedings of the Institution of Mechanical Engineers, Part A: Journal of Power and Energy*, vol. 225, no. 7, pp. 864–876, 2011.

[8] F. Dietmann and M. Casey, "The effects of reynolds number and roughness on compressor performance," in *10 th European Conference on Turbomachinery Fluid dynamics & Thermodynamics*, EUROPEAN TURBOMACHINERY SOCIETY, 2013.

[9] M. Heß and P. F. Pelz, "On reliable performance prediction of axial turbomachines," in *ASME Turbo Expo 2010: Power for Land, Sea, and Air*, pp. 139–149, American Society of Mechanical Engineers, GT2010-22290.

[10] J. Tiainen, A. Jaatinen-Värri, A. Grönman, and J. Backman, "Numerical study of the reynolds number effect on the centrifugal compressor performance and losses," in *ASME Turbo Expo 2016: Turbomachinery Technical Conference and Exposition*, pp. V02DT42A002–V02DT42A002, American Society of Mechanical Engineers, 2016.

[11] G.-C. Zha, B. F Carroll, C. D. Paxton, C. A. Conley, and A. Wells, "High-performance airfoil using coflow jet flow control," *AIAA Journal*, vol. 45, no. 8, pp. 2087–2090, 2007.

[12] A. Lefebvre, B. Dano, W. Bartow, M. Fronzo, and G. Zha, "Performance and energy expenditure of coflow jet airfoil with variation of mach number," *Journal of Aircraft*, vol. 53, no. 6, pp. 1757–1767, 2016.

[13] G. Zha, W. Gao, and C.D. Paxton, "Jet Effects on Co-Flow Jet Airfoil Performance," *AIAA Journal*, vol. 45, pp. 1222–1231, 2007.

[14] G.-C. Zha, C. Paxton, A. Conley, A. Wells, nd B. Carroll, "Effect of Injection Slot Size on High Performance Co-Flow Jet Airfoil," *AIAA Journal of Aircraft*, vol. 43, pp. 987–995, 2006.

[15] Yang, Yunchao and Zha, Gecheng, "Super-Lift Coefficient of Active Flow Control Airfoil: What is the Limit?," *AIAA SCITECH2017, 55th AIAA Aerospace Science Meeting, Grapevine, Texas*, AIAA 2017-1693.

[16] B. P. E. Dano, D. Kirk, and G.-C. Zha, "Experimental Investigation of Jet Mixing Mechanism of Co- Flow Jet Airfoil." AIAA-2010-4421, 5th AIAA Flow Control Conference, Chicago, IL, 28 Jun - 1 Jul 2010.

[17] B. Dano, G. Zha, and M. Castillo, "Experimental study of co-flow jet airfoil performance enhancement using discreet jets," in *49th AIAA Aerospace Sciences Meeting including the New Horizons Forum and Aerospace Exposition*, AIAA 2011-0941.

[18] Lefebvre, A. and Zha, G.-C. , "Design of High Wing Loading Compact Electric Airplane Utilizing Co-Flow Jet Flow Control." AIAA Paper 2015-0772, AIAA SciTech2015: 53nd Aerospace Sciences Meeting, Kissimmee, FL, 5-9 Jan 2015.

[19] Lefebvre, A. and Dano, B. and Bartow, W. and Di Franzo, M. and Zha, G.-C., "Performance Enhancement and Energy Expenditure of Co-Flow Jet Airfoil with Variation of Mach Number." AIAA Paper 2013-0490, AIAA Journal of Aircraft, DOI: 10.2514/1.C033113, 2016.

[20] Liu, Z.-X. and Zha, G.-C., "Transonic Airfoil Performance Enhancement Using Co-Flow Jet Active Flow Control." AIAA Paper 2016-3066, AIAA Aviation, June 13-17 2016.

[21] Lefebvre, A. and Zha, G.-C., "Trade Study of 3D Co-Flow Jet Wing for Cruise Performance." AIAA Paper 2016-0570, AIAA SCITECH2016, AIAA Aerospace Science Meeting, San Diego, CA, 4-8 January 2016.

[22] J. Zhang, K. Xu, Y. Yang, Y. Ren, P. Patel, and G. Zha, "Aircraft control surfaces using co-flow jet active flow control airfoil," in *2018 Applied Aerodynamics Conference*, AIAA 2018-3067.

[23] K. Xu, J. Zhang, and G. Zha, "Drag minimization of co-flow jet control surfaces at cruise conditions," in *AIAA Scitech 2019 Forum*, AIAA 2019-1848.

[24] C. Robison, "Design of a mixed flow fan," vol. PCA-211-3-rep1-1, PCA Engineering Limited, Feb. 23, 2017.

[25] C. Zwyssig, "Design of a mixed flow fan prototype," vol. PR-4241-011, Celereton, Oct. 24, 2017.

[26] X. Kewei and G.-C. Zha, "Design of High Specific Speed Mixed Flow Micro-Compressor for Co-flow Jet Actuators." ASME Paper GT2019-90980, ASME TURBO EXPO 2019, Phoenix, Arizona, USA, June 17-21, 2019.

[27] J. D. Denton, "Loss mechanisms in turbomachines," in *ASME 1993 International Gas Turbine and Aeroengine Congress and Exposition*, pp. V002T14A001–V002T14A001, American Society of Mechanical Engineers, 1993.